Received: 24 July 2018 | Accepted: 29 January 2019

DOI: 10.1002/pip.3121

RESEARCH ARTICLE

WILEY PROGRESS IN PHOTOVOLTAICS

Discriminating bulk versus interface shunts in organic solar cells by advanced imaging techniques

André Karl[1] | Andres Osvet[1] | Andreas Vetter[1,2] | Philipp Maisch[2] | Ning Li[1] | Hans-Joachim Egelhaaf[2] | Christoph J. Brabec[1,2]

[1] Institute of Materials for Electronics and Energy Technology (i-MEET), Friedrich-Alexander-University Erlangen-Nuremberg, Martensstraße 7, 91058 Erlangen, Germany

[2] Bavarian Center for Applied Energy Research (ZAE Bayern), Immerwahrstraße 2, 91058 Erlangen, Germany

Correspondence
André Karl, Institute of Materials for Electronics and Energy Technology (i-MEET), Friedrich-Alexander-University Erlangen-Nuremberg, Martensstraße 7, 91058 Erlangen, Germany.
Email: andre.karl@fau.de

Funding information
Deutsche Forschungsgemeinschaft (DFG), Grant/Award Number: BR 4031/6-1; Bavarian Ministry of Economic Affairs and Media, Energy and Technology

Abstract

An important aspect when upscaling organic photovoltaics from laboratory to industrial scale is quality control. Established imaging techniques like lock-in thermography or luminescence imaging are frequently used for this purpose. While these techniques allow for the lateral detection of defects, they cannot provide information on the vertical position of the defect in the OPV stack. Here, we present an approach to overcome this limitation. A femtosecond-laser is deployed to introduce well-defined artificial calibration defects selectively into both the interface and the bulk active layer of inverted P3HT:PCBM bulk heterojunction cells during device fabrication. The defective cells are then characterized using J-V analysis and several nondestructive imaging methods (dark lock-in thermography, photoluminescence, and electroluminescence imaging). The distinct response for each defect in the different imaging methods enables us to uniquely distinguish between bulk and interface defects. This allows to study surface recombination under most controlled conditions.

KEYWORDS

dark lock-in thermography, electroluminescence, imaging, organic solar cells, photoluminescence, quality control

1 | INTRODUCTION

In recent years, the field of organic photovoltaics (OPV) has made significant progress increasing the efficiency of OPV devices to over 10%.[1-5] This, combined with its many desirable properties, like solution processability or the possibility of printing semitransparent or flexible devices, has made OPV increasingly interesting as a scalable module technology for building integrated photovoltaics.[6-8] One of the challenges when upscaling an established laboratory method toward industrial scale is the quality control on large areas. While standard characterization methods like recording of J-V curves or EQE measurements can provide valuable information about the type of defects, they cannot provide information about the location or origin of defects.

To gain this information, imaging characterization techniques, most prominently lock-in thermography (LIT) and luminescence imaging, can be employed for nondestructive characterization. Lock-in thermography measures the temperature distribution of a sample under load, either with electrical excitation (dark lock-in thermography—DLIT) or with optical excitation (illuminated lock-in thermography—ILIT). Lock-in thermography shows localized spots of high power dissipation, usually shunts, as such spots show increased temperature as compared with the rest of the sample under load.[9,10] Luminescence imaging on the other hand shows the spatial distribution of luminescence intensity, ie, radiative recombination, on a device, either by investigating the electroluminescence of a sample (EL imaging) or the photoluminescence of a sample (PL imaging).[11-13] Using different excitation methods may yield quantitatively and qualitatively different results because EL is sensitive to the charge extraction/injection into the active layer (AL) as well as to the integrity of the AL itself, while PL only probes the AL.[14,15] Luminescence imaging and LIT have been

used for characterization of both classic crystalline silicon photovoltaics[16-18] as well as characterization of novel thin-film photovoltaics like OPV[19-22] or hybrid perovskite solar cells.[23-25]

Visualizing the position of defects is the major strength of imaging methods; however, depth resolution allowing the determination of the vertical position of a defect (ie, in which layer of the thin-film device a defect is located) is majorly limited. This impedes the differentiation of defects in multilayer architectures. For example, classical DLIT uniquely evidences the existence of shunts but does not provide information whether the shunt is in the interface layers or in the bulk AL. However, this information is critically required to correlate the occurrence of defects with the quality of single processing steps during fabrication. Detailed knowledge of the vertical location of defects allows the target-oriented development of quality control methods, which becomes more and more important with the increasing complexity of high-performance solar cells, eg, tandem solar cells.

In this manuscript, we suggest an innovative concept to more fundamentally address this problem. By the introduction of artificial reference defects into the single layers of an OPV device, we successively correlate differently positioned defects to their corresponding layers. Based on the correct defect allocation, it allows establishing a calibration routine for the various imaging methods to become sensitive to the vertical position of defects. The approach of introducing calibration defects has already been successfully applied for assessing the accuracy of a single imaging method. Augarten et al used such an approach for silicon solar cells and PL imaging,[26] while Vetter et al applied ILIT imaging for the calibration of CIGS solar cells.[27]

Femtosecond laser patterning allows to introduce well-defined defects in the single layers of an OPV cell which then can be characterized by various imaging techniques. The principles of the fs-laser process for introducing artificial defects are similar to the ones used for fabricating high-resolution OPV modules.[28,29] This allowed us to calibrate the imaging technique to the vertical position within an OPV stack. After successfully calibrating the imaging technique to artificial defects, we further characterized samples with naturally occurring defects and allocated them to the single layers. The principles of that procedure are schematically summarized in Figure 1.

We applied this method to differentiate between defects in interface and bulk layers of inverted P3HT:PCBM organic bulk-heterojunction (BHJ) solar cells. The P3HT:PCBM system is one of most extensively studied OPV systems available with reasonable efficiency and excellent stability.[30,31] The stability of this system is further improved by employing an inverted device structure,[32,33] with ITO as the anode and a high work function metal, eg, silver, as the cathode.

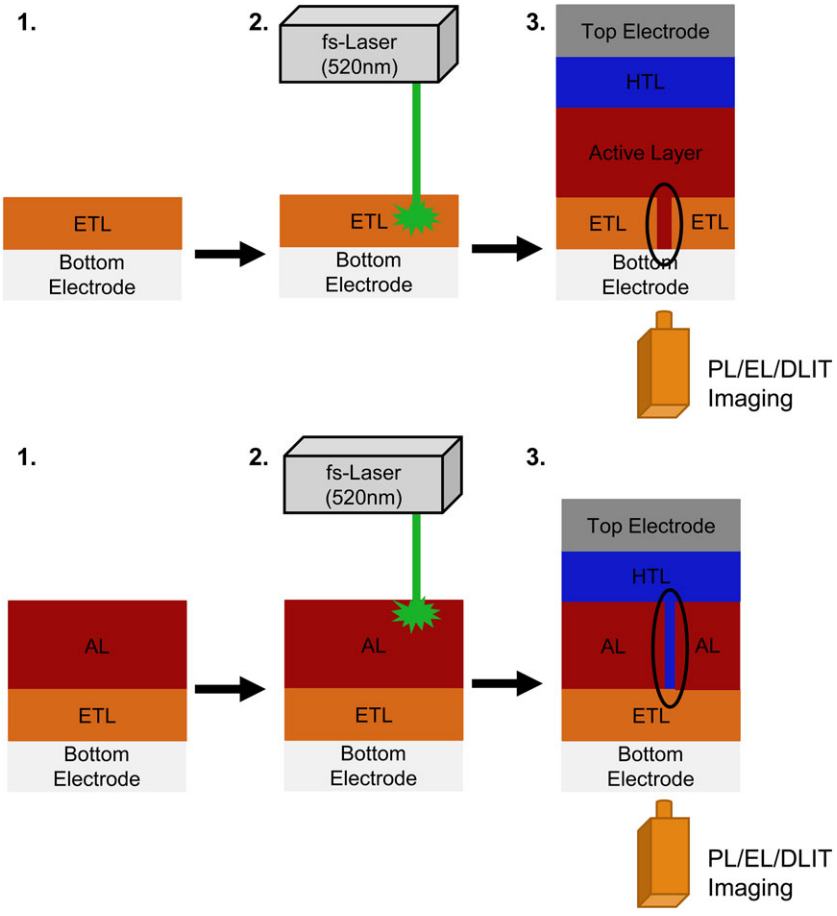

FIGURE 1 Schematic of the introduction of artificial defects using a fs-laser into two different layers (top: ETL; bottom: AL) of an OPV device. First, the cell is processed up to the desired layer. After that, a defect is introduced into that layer by fs-laser ablation. As the last step, the fabrication of the cell is completed, and the sample is analyzed by various imaging methods [Colour figure can be viewed at wileyonlinelibrary.com]

2 | RESULTS AND DISCUSSION

2.1 | Laser ablation experiments

Introducing highly defined defects into selective solar cell layers by laser ablation requires the determination of the ablation parameters for single materials. Each layer combination (pristine ITO, ZnO on ITO, P3HT:PCBM on ZnO/ITO and PEDOT:PSS [AL 4083, Heraeus] on P3HT:PCBM/ZnO/ITO) was prepared identically to regular solar cell fabrication. Single shot ablation thresholds were determined for every layer, in order to determine the ablation threshold fluence (except for the top electrode).[29,34,35] The ablation threshold fluence can be determined from the correlation between the squared diameter of the ablated spot by a single shot and the used laser fluence:

$$D^2 = 2\omega_0^2 \ln\left(\frac{F}{F_{th}}\right) \quad (1)$$

with ω_0 as the radius of the laser beam on the surface, D^2 as the squared diameter of the ablated spot, F as the laser fluence, and F_{th} as the threshold fluence. F_{th} can now be determined from the intersection of a linear fit in a semilogarithmic plot of D^2 against the laser fluence (Figure 2). The values for the ablation threshold fluence (Table 1) for the layers show that the removal of the ZnO and P3HT:PCBM should be possible without damaging the underlying layers. ZnO on top of ITO can be removed at laser fluences between 0.42 and 0.27 J*cm^{-2} without damaging ITO. Fluences between 0.12 and 0.27 J*cm^{-2} can be used to selectively remove P3HT:PCBM. For the PEDOT:PSS layer, it seems that it could be selectively removed without damaging the underlying AL. However, because the PEDOT:PSS film has a transmission of over 90% at 520 nm,[36] the PEDOT:PSS film is only removed by the ablation of the underlying AL, which is obvious from the appearance of the ablated area (Figure S1). Thus, the ablation threshold measurement shows rather the ablation thresholds for the complete stack instead of the ablation threshold for the PEDOT:PSS layer only. Based on these results, a laser fluence of ca. 0.13 J*cm^{-2} was chosen for removing the P3HT:PCBM layer, and a laser fluence of 0.39 J*cm^{-2} was chosen for removing the ZnO layer.

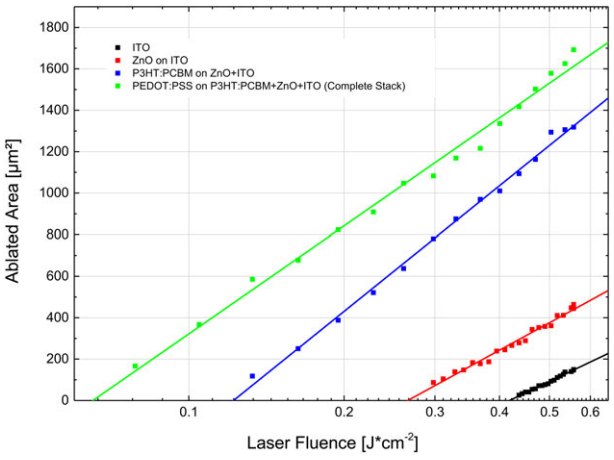

FIGURE 2 Ablation threshold measurements for single layers in an inverted P3HT:PCBM bulk heterojunction solar cell [Colour figure can be viewed at wileyonlinelibrary.com]

TABLE 1 Values for the ablation threshold fluence for each layer

Material	Threshold Fluence, J*cm^{-2}
ITO	0.42
ZnO (on ITO)	0.27
P3HT:PCBM (on ITO and ZnO)	0.12
PEDOT:PSS (on P3HT:PCBM, ZnO, and ITO)	0.07

Another important parameter controlling laser ablation of thin layers is the overlap between single laser pulses as well as the number of passes. After a series of tests, best results were obtained by using a pulse overlap of 50% for removing ZnO and an overlap of 77.5% for removing P3HT:PCBM. At least two passes were required to ensure complete removal of the material. To confirm complete removal, a 500-µm-wide stripe of the P3HT:PCBM was removed first, and subsequently a 250-µm-wide stripe of ZnO was removed. The areas were further examined with an optical microscope and a profilometer (Figure 3). The optical microscope image shows different contrast for the separately patterned areas which we accounted to the AL, ZnO, and ITO (see Figure 3A). The profilometer shows an approximately 400-nm step between the top of the AL and the ETL, and an approximately 30 to 40-nm step between the top of the ETL and the bottom electrode. This is in excellent agreement with the true height of these layers. The integrity of ITO was confirmed by a resistance measurement on the bare area. No significant difference to a pristine ITO sample was observed.

2.2 | ETL (ZnO) defects

To test the influence of defects in the ETL on the solar cell performance and the appearance of the cells in different imaging methods, inverted P3HT:PCBM solar cells with one to three defects were fabricated (Figure 4). After coating the ETL, circular areas with a radius of d = 400 µm were removed to introduce defects in which the AL has direct contact to the bottom electrode. Regular cell processing was finished after defect assembly. Additionally to the three defective cells, three intact reference cells were fabricated on the same sample in order to have the best possible comparison between defective and nondefective cells.

J-V curves were recorded in order to see whether the 400-micron sized ETL defects influence the electrical parameters of 10.4-mm^2 cells (Figure 5). Comparing the curves of a cell with and without a defect on the same substrate, there is little to no difference visible in both the illuminated and the dark J-V curves. None of the major electrical parameters of the solar cell (V_{oc}, J_{sc}, FF, and PCE) seem to be impacted (Table 2). Furthermore, the introduction of up to three defects still does not have any more significant influence on the performance of the cell. Because these defects are already <1% of the cell area per defect, we conclude that interface defects which lead to a direct contact between the ITO bottom electrode and the AL do not cause any major power dissipation for this system.

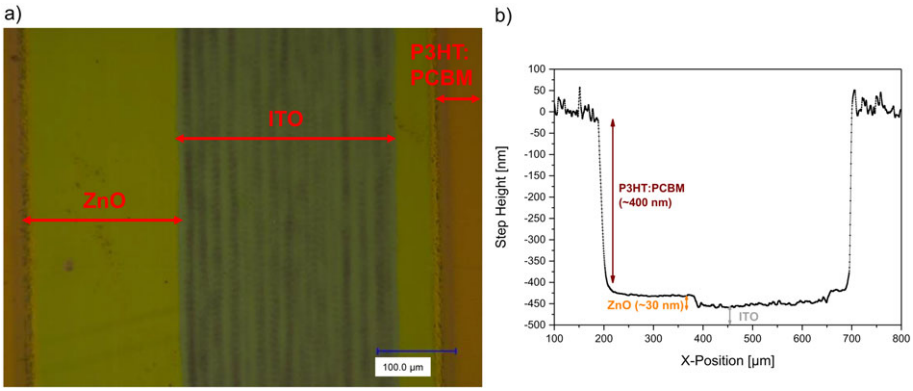

FIGURE 3 A, Optical microscope image of a sample with ITO/ZnO/P3HT:PCBM stack with a removed stripe of P3HT:PCBM and a removed stripe of ZnO; B, profile line over the section seen in the microscope image [Colour figure can be viewed at wileyonlinelibrary.com]

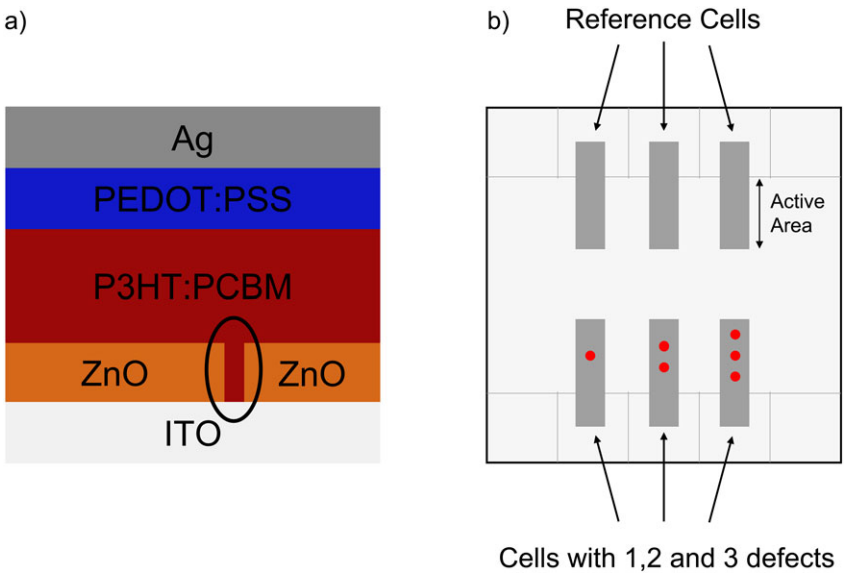

FIGURE 4 A, Schematic of inverted P3HT:PCBM cells with an ETL defect; B, cell layout used for introduction of defects [Colour figure can be viewed at wileyonlinelibrary.com]

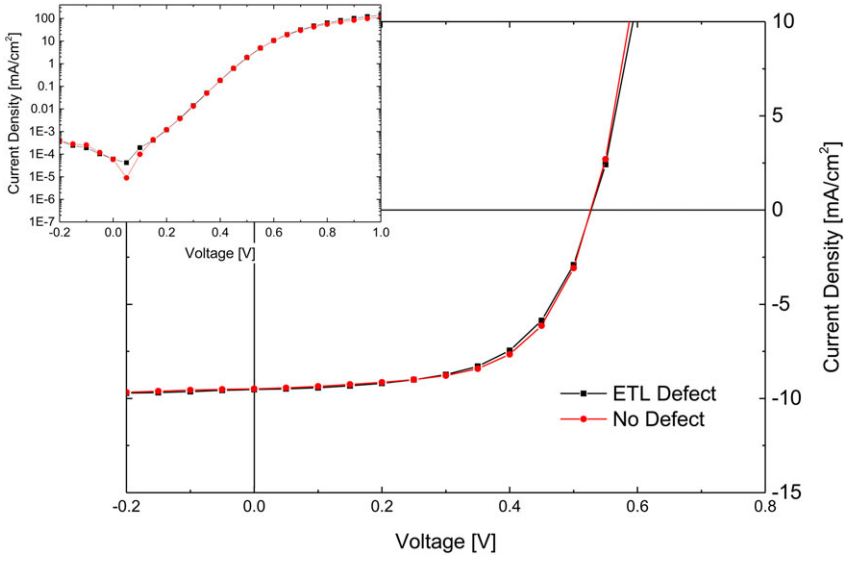

FIGURE 5 Illuminated and dark J-V curves for an inverted P3HT:PCBM cell with and without an ETL defect [Colour figure can be viewed at wileyonlinelibrary.com]

TABLE 2 Electrical parameters for inverted P3HT:PCBM cells with 0, 1, and 3 ETL defects

	V_{oc}, V	J_{sc}, mA/cm^2	FF, %	PCE, %
No defects	0.53	9.49	60.94	3.07
1 defect (r = 200 µm)	0.53	9.54	59.14	2.99
3 defects (r = 200 µm)	0.53	9.35	59.18	2.93

Additionally to electrical characterization, defective cells were investigated using EL imaging, PL imaging, and DLIT to identify their fingerprint for the various imaging techniques (Figure 6). Looking at the EL image, the ETL defect is clearly visible as a dark spot with a lower electroluminescence intensity compared with rest of the cell. Because electroluminescence is sensitive to both charge injection across the interfaces as well as the integrity of the AL, PL imaging is required to exclusively verify the integrity of the AL.[14,15] Because the AL has not been damaged during cell production, the PL image shows a homogeneous distribution of PL signal over the whole cell area. A minor decrease in PL intensity at the position of the defect is rather attributed to minor optical changes and/or slight differences in AL thickness caused by the removal of the ETL. We conclude that the removal of the ETL causes an increased injection barrier for electrons between the AL and the ITO cathode. The electron injection barrier for the ITO/AL interface is expected to be much higher than for the ITO/ZnO/AL interface. The reduced charge injection thus leads to a reduction of EL intensity at the defect position. DLIT, unlike EL imaging and PL imaging, does not probe radiative recombination of the solar cell but rather images dissipation of heat as caused by carrier recombination or parasitic ohmic or non-ohmic shunts.[37] The DLIT image of a cell with an ETL defect shows reduced heat dissipation at the position of the defect. This is in good agreement with the information from the J-V curves, which suggested that this type of defect negligibly influences cell performance. The reduced heat dissipation at the defect spot is again attributed to locally inhibited charge injection, similar to the reason why the EL intensity is lower at the defect position.

Because the introduction of up to three defects into the ETL did not show a significant influence on the cell performance, samples with higher amount of defects were fabricated. Samples with 0, 1, 3, 5, 10, and 15 defects with a diameter of 400 µm were produced, corresponding to a total percentage of defective cell area between 1.2% (1 defect) and 18.2% (15 defects). As discussed before, the electrical parameters for up to three defects are relatively stable. However, samples with a larger number of defects show a distinctly steady decrease in fill factor, V_{oc}, and consequently power conversion efficiency (Figure 7). This is most likely due to the inhibited charge extraction and increased nonradiative surface recombination at the position of the defects due to the missing ETL. Furthermore, the stability of J_{sc} with an increasing number of defects shows that defected areas still produce photocurrent under the built-in field and are not negatively impacted by the introduction of the laser defects.

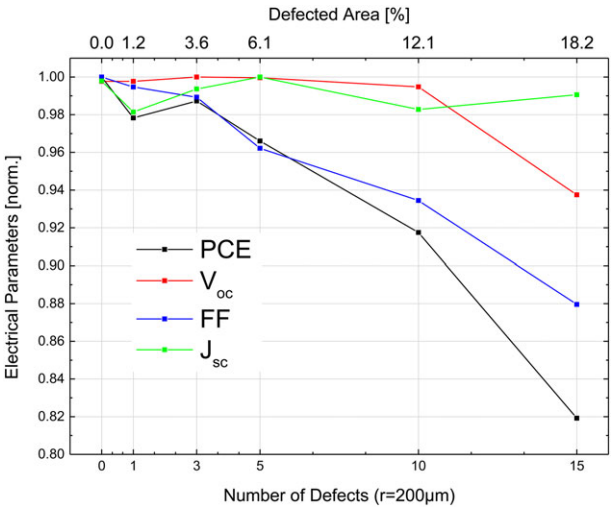

FIGURE 7 Normalized electrical parameters of inverted P3HT:PCBM cells with increasing amounts of defects in the ETL layer [Colour figure can be viewed at wileyonlinelibrary.com]

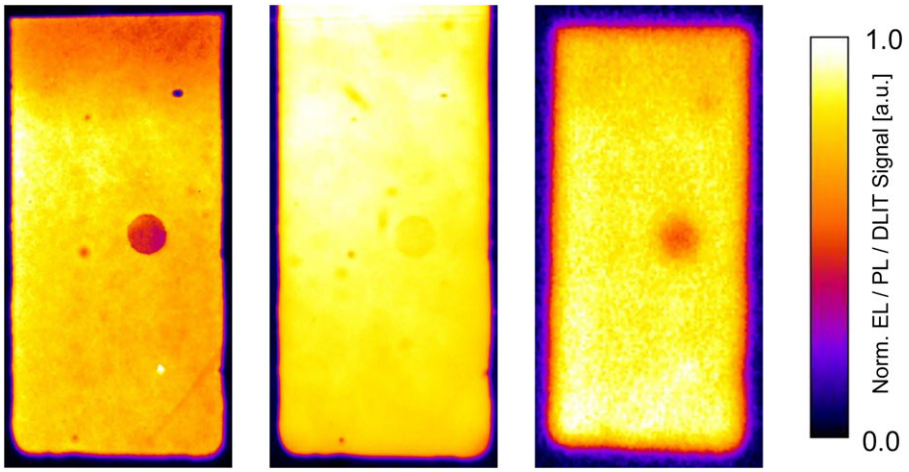

FIGURE 6 From left to right: EL, PL, and DLIT image of an inverted P3HT:PCBM cell with a defect in the ETL layer [Colour figure can be viewed at wileyonlinelibrary.com]

Next, we looked into the HTL (PEDOT:PSS). As PEDOT:PSS could not be selectively laser-removed without damaging the AL, we developed a different strategy to introduce defects into the top HTL. Inkjet printing was employed to print PEDOT:PSS (FHC, Heraeus) layers with well-defined pinholes. Larger defects were introduced using a masked doctor blade, leaving a stripe of the sample uncoated by PEDOT:PSS. We found defects introduced in the HTL to behave identical as the defects in the ETL. A decreased EL/DLIT signal at the position of the defects (Figure S2) is accompanied by a negligible decrease of the photovoltaic parameters for up to 5% defective area (Figure S3 + S4). V_{oc}, FF, and PCE again become more strongly affected for a defective area is larger than about 5% of the total cell area. In general, we found the inkjet procedure being slightly less attractive and reproducible as the defect area is larger and less precisely controlled. Nevertheless, the observations are qualitatively and quantitatively comparable to the ones for the ETL defects.

2.3 | Active layer (P3HT:PCBM) defects

Besides defects in both interface layers, artificial defects were introduced into the P3HT: PCBM bulk AL as well. The expected behavior for such defects resembles the one of a "classic" shunt offering an alternative low ohmic current path between the charge injection layers. Preliminary tests revealed a dramatic impact of AL defects on the performance of the solar cell, forcing us to reduce the defect geometry from 400-µm-sized circular spots to elliptical spots with a length of 75 µm and a width of 30 µm, which was limited by the laser spot diameter of 44 µm at $1/e^2$ intensity (Figure S5). Samples with defects in the AL were processed with a 10-nm evaporated MoO_3 layer as HTL instead of PEDOT:PSS. This was done to ensure that the ZnO layer, which is exposed after removal of the AL, is not dissolved by the PEDOT:PSS solution.

The J-V curves of samples with an elliptical defect in the AL (Figure 8) show that the V_{oc}, FF, and PCE are significantly decreased (Table 3). R_{sh}, estimated from the slope of the J-V curves around 0 V, is drastically reduced by ca. 2 orders of magnitude as well (from ca. 8370 Ω*cm^2 to ca. 84.8 Ω*cm^2). Accordingly, our artificially introduced defect resembles an ohmic shunt in the solar cell.

Both EL and PL images show a dark spot in the form of the removed elliptical spot at the position of the defect (Figure 9) as the AL is the only source for radiative recombination. The DLIT image (Figure 10) on the other hand shows a strong signal at the defect position, which imposes that a hot spot has formed. While in the EL and PL images, the defect size is exactly that of the ablated elliptical

TABLE 3 Electrical parameters for inverted P3HT:PCBM cells with 0, 1, and 3 AL defects

	V_{oc}, V	J_{sc}, mA/cm^2	FF, %	PCE, %
No defects	0.53	10.09	63.88	3.41
1 defect	0.47	10.13	36.07	1.71
3 defects	0.08	9.63	25.59	0.19

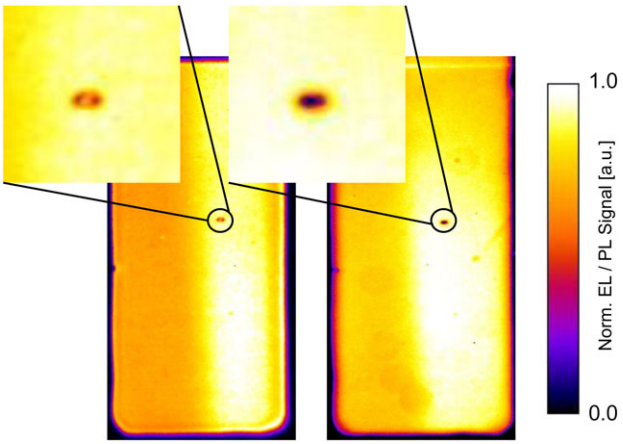

FIGURE 9 EL (left) and PL (right) image of an inverted P3HT:PCBM cell with a defect in the AL. The defects are highlighted by the black circle [Colour figure can be viewed at wileyonlinelibrary.com]

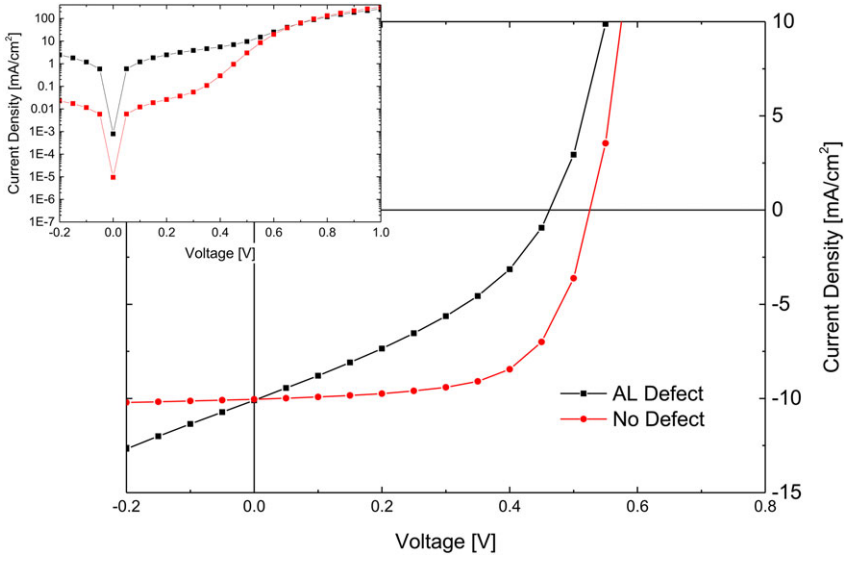

FIGURE 8 Illuminated and dark J-V curves for an inverted P3HT:PCBM cell with and without an AL defect [Colour figure can be viewed at wileyonlinelibrary.com]

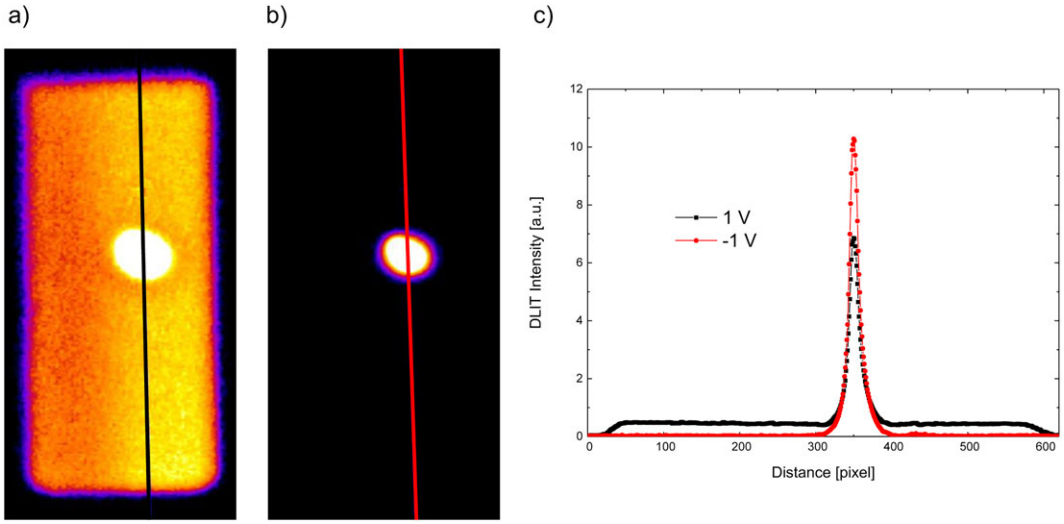

FIGURE 10 A, DLIT image of an inverted P3HT:PCBM cell with a defect in the AL under forward bias (1 V); B, DLIT image of the same cell under reverse bias (−1 V); and C, profile line across the cell area at forward and reverse bias [Colour figure can be viewed at wileyonlinelibrary.com]

spot, the defect appears much larger in the DLIT image due to diffusion of the heat at the hot spot. The formation of hot spots is typically associated with the formation of a shunt in the solar cell, as observed here. The injected charge carriers can directly thermally recombine at the interface between the HTL and the ETL leading to heat dissipation at the defect. The decrease in R_{sh} leads to a dramatic reduction of V_{oc}, FF, and PCE. Additionally to the DLIT image under forward bias, a DLIT image under reverse bias was recorded as well. The reverse bias image shows the same signal as under forward bias image at the defect position, which uniquely proves the presence of an ohmic shunt.

3 | CONCLUSION

In summary, well-defined artificial defects have been introduced into the bulk AL and the interface layers of inverted P3HT:PCBM BHJ solar cells using a fs-laser. The cells have been characterized using standard electrical characterization tools, which showed that AL defects have a strong effect on the solar cell performance, while interface defects have rather minor effects unless large areas (more than 5% of the cell area) are affected. The combination of three imaging techniques, namely DLIT and luminescence imaging with both optical and electrical excitation, uniquely allows to distinguish AL defects from bulk defects. The assignment of defects to characteristic features in images allows to fingerprint them. Such knowhow on interpreting images is essential to develop fast, reliable, and nondestructive quality control methods for OPV manufacturing, which can spatially resolve a defect in all three dimensions.

4 | EXPERIMENTAL DETAILS

Solar cell preparation and characterization: The solar cells were prepared on ITO-covered glass (25 mm × 25 mm × 1.25 mm). First, the glass slides were cleaned for 10 minutes each in an ultrasonic bath with isopropanol and acetone. After blow drying the substrates, a ZnO nanoparticle solution (N10, Avantama) was coated on top of ITO using doctor blading in ambient atmosphere. After annealing the samples for 5 minutes at 80°C, the AL solution was applied, again using doctor blading in ambient atmosphere. The AL solution consists of a 1:1 blend of P3HT (Merck) and $PC_{60}BM$ (Solenne BV) at a concentration of 3.5 wt % in chlorobenzene with 5% p-bromoanisole as an additive.[38] After applying the AL, a hole transporting layer of PEDOT:PSS (AL 4083 or FHC, Heraeus) was applied by doctor blading (for cells with induced AL defects, a 10-nm layer of MoO_3 was evaporated instead of PEDOT:PSS). The whole stack was annealed in a nitrogen atmosphere for 5 minutes at 140°C. As last step, a 100-nm layer of silver was evaporated as top electrode. The active cell area of the cells was about 10.4 mm^2. Finished devices were glass-glass encapsulated with an UV-curable adhesive (DELO Katiobond LP 655, Delo, Windach, Germany).

The J-V characteristics of the cells were measured with an Oriel Sol 1 A solar simulator from Newport (Irvine, California, United States) under AM 1.5G irradiation. The light source was calibrated with a reference silicon solar cell. All cells were measured under ambient condition.

For the investigation of the ablated areas, an optical microscope, VHX-2000 from Keyence (Osaka, Japan), and a Profilometer, AlphaStep D-500 Stylus Profiler from KLA Tencor (Milpitas, California, United States), were used.

Imaging: For DLIT measurements, an Equus 327 kNM camera from IRcam GmbH (Erlangen, Germany) was used. The camera is equipped with a Stirling cooled Indium-Antimonide (InSb) focal plane array detector (640 × 512) which is sensitive between 1 and 5 µm. For EL and PL imaging, a Ninox VIS-SWIR 640 camera from Raptor Photonics (Milbrook, Northern Ireland) was used. The camera is equipped with an air-cooled extended indium-gallium-arsenide detector (InGaAs) which is sensitive between 0.4 and 1.7 µm.

Excitation for DLIT and EL imaging was carried out with a Keysight B2901A Precision Source/Measure Unit from Keysight Technologies, Inc. (Santa Rosa, California, United States). In case of DLIT, a lock-in frequency of 10 Hz with an integration time of 1 ms was used. EL images were measured with an integration time of 2000 ms and corrected for the background.

Excitation for PL imaging was carried out with a RLTMGL-532-2.5 W 532-nm fiber coupled laser diode (ROITHNER LASERTECHNIK GmbH) with a maximum output power of 2.5 W. After accounting for all optical losses from beam expansion to an area of about 20 cm^2, a total power density of ~ 0.5 Wcm^{-2} was measured on the surface. An integration time of 250 ms was used. In addition to a background correction (subtraction of the image without illumination), a flat-field correction was performed to account for typical deviations in illumination intensity (± 10%).

Laser source for introduction of defects: The ETL and AL defects were introduced using an "LS 7xxP" Setup (LS Laser Systems GmbH) using a "femtoREGENTM UC-1040-8000 fs Yb SHG" laser source (High Q Laser GmbH). The laser has a fundamental wavelength of 1040 nm but was operated at 520 nm using SHG. The pulse duration is <350 fs at repetition rates of up to 960 kHz. The laser has a beam quality of M^2 < 1.25 (@ 1040 nm), M^2 < 1.5 (@ 520 nm) and a pulse-to-pulse stability of <2% for both wavelengths. The beam is moved over the sample surface using a galvanometer-mounted mirror, allowing for patterning speeds of up to 4000 mm/s.

ACKNOWLEDGEMENTS

This work was financially supported by the Deutsche Forschungsgemeinschaft (DFG) research grant: BR 4031/6-1, "Entwicklung von bildgebenden Verfahren zur Defekterkennung in Tandem Solarzellen". N.L. gratefully acknowledges the financial support from the DFG research grant: BR 4031/13-1, and the Bavarian Ministry of Economic Affairs and Media, Energy and Technology by funding the HI-ERN (IEK11) of FZ Jülich. C.J.B. gratefully acknowledges the financial support through the "Aufbruch Bayern" initiative of the state of Bavaria (EnCN and "Solar Factory of the Future"), the Bavarian Initiative "Solar Technologies go Hybrid" (SolTech), and the SFB 953 (DFG). The Bavarian State Government is acknowledged for financial support of the "Solar Factory of the Future" as part of the Energy Campus Nuremberg (FKZ 20.2-3410.5-4-5).

ORCID

André Karl https://orcid.org/0000-0003-2289-5987

REFERENCES

1. Zhao W, Li S, Yao H, et al. Molecular optimization enables over 13% efficiency in organic solar cells. *J Am Chem Soc*. 2017;139(21):7148-7151.
2. De Chen J, Cui C, Li YQ, et al. Single-junction polymer solar cells exceeding 10% power conversion efficiency. *Adv Mater*. 2015;27(6):1035-1041.
3. Gasparini N, Lucera L, Salvador M, et al. High-performance ternary organic solar cells with thick active layer exceeding 11% efficiency. *Energ Environ Sci*. 2017;10(4):885-892.
4. Lu L, Zheng T, Wu Q, Schneider AM, Zhao D, Yu L. Recent advances in bulk heterojunction polymer solar cells. *Chem Rev*. 2015;115(23):12666-12731.
5. Green MA, Hishikawa Y, Warta W, et al. Solar cell efficiency tables (version 50). *Prog Photovoltaics Res Appl*. 2017;25(7):668-676.
6. Hoppe H, Sariciftci N. Organic solar cells: an overview. *J Mater Res*. 2004;19(07):1924-1945.
7. Li N, Baran D, Spyropoulos GD, et al. Environmentally printing efficient organic tandem solar cells with high fill factors: a guideline towards 20% power conversion efficiency. *Adv. Energy Mater*. 2014;4(11):140e0084.
8. Krebs FC. Fabrication and processing of polymer solar cells: a review of printing and coating techniques. *Sol. Energy Mater. Sol. Cells*. 2009;93(4):394-412.
9. Breitenstein O. Illuminated versus dark lock-in thermography investigations of solar cells. *Int J Nanoparticles*. 2013;6(2/3):81.
10. Bauer J, Breitenstein O, Wagner J. Electron. Device fail. *Analyst*. 2009;11:6.
11. Kasemann M, Grote D, Walter B, et al. Luminescence imaging for the detection of shunts on silicon solar cells. *Prog Photovolt Res Appl*. 2008;16(4):297-305.
12. Breitenstein O, Bauer J, Trupke T, Bardos RA. On the detection of shunts in silicon solar cells by photo- and electroluminescence imaging. *Prog. Photovoltaics Res. Appl.* 2008;16(4):325-330.
13. Breitenstein O, Bauer J, Bothe K, et al. *A L Thermography*. 2011;1:159.
14. Adams J, Salvador M, Lucera L, et al. *Adv. Energy Mater*. 2015;5.
15. Seeland M, Rösch R, Hoppe H. *J Appl Phys*. 2011;109:1.
16. Trupke T, Bardos RA, Schubert MC, Warta W. Photoluminescence imaging of silicon wafers. *Appl Phys Lett*. 2006;89(4):44107.
17. Breitenstein O, Rakotoniaina JP, Al Rifai MH, Werner M. Shunt types in crystalline silicon solar cells. *Prog. Photovoltaics Res. Appl.* 2004;12(7):529-538.
18. Spataru S., Hacke P., Sera D., Glick S., Kerekes T., Teodorescu R., in 2015 *IEEE 42nd Photovolt. Spec. Conf*., IEEE, 2015, pp. 1–6.
19. Bachmann J, Buerhop-Lutz C, Deibel C, et al. Organic solar cells characterized by dark lock-in thermography. *Sol. Energy Mater. Sol. Cells*. 2010;94(4):642-647.
20. Hoyer U, Wagner M, Swonke T, et al. *Appl Phys Lett*. 2010;97:13.
21. Rösch R, Krebs FC, Tanenbaum DM, Hoppe H. Quality control of roll-to-roll processed polymer solar modules by complementary imaging methods. *Sol. Energy Mater. Sol. Cells*. 2012;97:176-180.
22. Besold S, Hoyer U, Bachmann J, et al. Quantitative imaging of shunts in organic photovoltaic modules using lock-in thermography. *Sol. Energy Mater. Sol. Cells*. 2014;124:133-137.
23. Hameiri Z, Mahboubi Soufiani A, Juhl MK, et al. Photoluminescence and electroluminescence imaging of perovskite solar cells. *Prog. Photovolt Res. Appl*. 2015;23(12):1697-1705.
24. Soufiani AM, Tayebjee MJY, Meyer S, et al. Electro- and photoluminescence imaging as fast screening technique of the layer uniformity and device degradation in planar perovskite solar cells. *J Appl Phys*. 2016;120(3):35702.
25. Soufiani AM, Hameiri Z, Meyer S, et al. *Adv Energy Mater*. 2017;7:1.
26. Augarten Y, Trupke T, Lenio M, et al. *Prog. Photovoltaics Res. Appl.* 2013;21:933.
27. Vetter A, Babbe FS, Hofbeck B, et al. Visualizing the performance loss of solar cells by IR thermography—an evaluation study on CIGS with artificially induced defects. *Prog. Photovoltaics Res. Appl.* 2016;24(7):1001-1008.

28. Spyropoulos GD, Kubis P, Li N, et al. Flexible organic tandem solar modules with 6% efficiency: combining roll-to-roll compatible processing with high geometric fill factors. *Energ Environ Sci*. 2014;7(10):3284-3290.
29. Kubis P, Li N, Stubhan T, et al. Patterning of organic photovoltaic modules by ultrafast laser. *Prog. Photovoltaics Res. Appl.* 2015;23(2):238-246.
30. Dennler G, Scharber MC, Brabec CJ. Polymer-fullerene bulk-heterojunction solar cells. *Adv Mater*. 2009;21(13):1323-1338.
31. Dang MT, Hirsch L, Wantz G. P3HT:PCBM, best seller in polymer photovoltaic research. *Adv Mater*. 2011;23(31):3597-3602.
32. Hau SK, Yip HL, Baek NS, Zou J, O'Malley K, Jen AKY. *Appl Phys Lett*. 2008;92:2006.
33. Kuwabara T, Nakayama T, Uozumi K, Yamaguchi T, Takahashi K. Highly durable inverted-type organic solar cell using amorphous titanium oxide as electron collection electrode inserted between ITO and organic layer. *Sol Energy Mater Sol Cells*. 2008;92(11):1476-1482.
34. Heise G, Trappendreher D, Ilchmann F, Weiss RS, Wolf B, Huber H. Picosecond laser structuring of thin film platinum layers covered with tantalum pentoxide isolation. *J Appl Phys*. 2012;112(1):13110.
35. Matylitsky V. V., Huber H., Kopf D., *30th Int. Congr. Appl. Lasers Electro-Optics, ICALEO* 2011 2011.
36. Xiao S, Abreu Fernandes S, Esen C, Ostendorf A, Laser Micro J. *Nanoeng*. 2011;6:249.
37. Hoppe H, Bachmann J, Muhsin B, et al. Quality control of polymer solar modules by lock-in thermography. *J Appl Phys*. 2010;107(1):14505.
38. Liu X, Huettner S, Rong Z, Sommer M, Friend RH. Solvent additive control of morphology and crystallization in semiconducting polymer blends. *Adv Mater*. 2012;24(5):669-674.

SUPPORTING INFORMATION

Additional supporting information may be found online in the Supporting Information section at the end of the article.

How to cite this article: Karl A, Osvet A, Vetter A, et al. Discriminating bulk versus interface shunts in organic solar cells by advanced imaging techniques. *Prog Photovolt Res Appl*. 2019;27:460–468. https://doi.org/10.1002/pip.3121